

Transmission and reflection of light in PTFE for Dark Matter research

1 Summary

Polytetrafluoroethylene (PTFE), commonly known by its brand name Teflon, is extensively employed in rare event searches, including Dark Matter (DM) research. Indeed, in DM experiments, PTFE reflectors are widely used to surround Liquid Xenon (LXe) detectors, as PTFE excellent diffuse reflectivity allows to efficiently collect the Vacuum Ultra-Violet scintillation light (~ 178 nm) emitted by LXe. The critical influence of reflectivity on detector performance, along with the growing interest in assembling thinner PTFE detector walls that maintain high collection efficiency while minimizing light leakages, motivates the need for accurate knowledge of PTFE transmittance (T) and reflectance (R), and of their dependence on PTFE thickness. In this work, a C++/ROOT pulse analysis software is developed to determine T and R at the PTFE–air interface. Measurements are performed by using a blue LED light source and PTFE discs of varying thicknesses (from 0.20 ± 0.05 mm to 5.15 ± 0.05 mm) at incidence and reflection angles of 30° , 45° and 60° . Attenuation coefficients are consistent across angles ($\lambda_T^{30^\circ} = (1.32 \pm 0.12)$ mm, $\lambda_T^{45^\circ} = (1.33 \pm 0.12)$ mm and $\lambda_T^{60^\circ} = (1.33 \pm 0.13)$ mm), while R shows a strong angular dependence. These results will contribute to the future development of ALPINE detector, whose LXe TPC features a novel PTFE–metal–PTFE interface with light-tight properties yet to be comprehensively characterized.

2 Project details

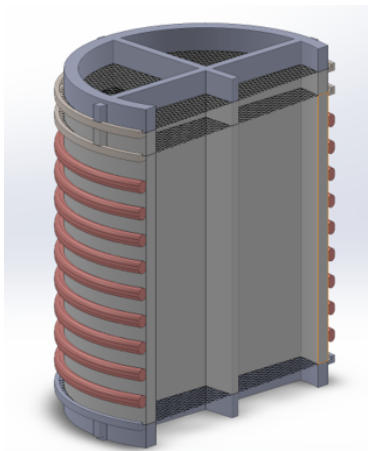
2.1 State-of-the-art and objectives

Observations at astrophysical and cosmological scales indicate that the ordinary visible matter alone is insufficient to describe the entire range of gravitational phenomena characterizing the Universe [1, 2]. This motivated the postulation of Dark Matter (DM), a non-visible form of mass which currently represents the most convincing framework for explaining the observed anomalies of the Universe [3]. The largest class of DM candidates consists of Weakly Interacting Massive Particles (WIMPs), which interact only via gravitational and weak forces [4]. Experiments employing direct detection techniques aim to observe WIMPs scattering off target nuclei, a process which produces measurable signals including the emission of scintillation light, which results from the de-excitation of scattered target atoms.

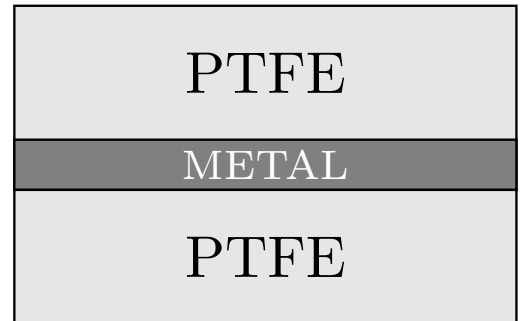
Liquid Xenon (LXe) detectors have proved ideal to reconstruct such scintillation signal due to their large mass, optical transparency and fiducialization [5–7]. Specifically, LXe scintillation light is centered in the Vacuum Ultra-Violet (VUV) wavelength at ~ 178 nm [8, 9], with its collection efficiency strongly affecting LXe detector performances. To maximize light collection efficiency, LXe volumes are enclosed in reflectors made of PTFE (Polytetrafluoroethylene)¹ [10] due to its excellent diffuse reflectivity, being $\sim 99\%$ in the visible and near infrared regions and $\sim 97\%$ at the VUV wavelength when immersed in LXe [11–13].

Precise knowledge of PTFE reflectance is crucial, as even tiny variations in reflectivity can critically affect the sensitivity of LXe detectors. In addition, considerable interest is devoted to the dependence of reflectivity on PTFE thickness, driven by the desire to reduce PTFE material in order to minimize dead volume, outgassing and radioactive background while still ensuring high light collection efficiency [14]. Conversely, a lower limit on PTFE thickness is set by its transmittance properties, as sufficient optical isolation is required to prevent light leakages and losses across the detector walls [15].

The primary objective of this work is to present angle-resolved transmittance (T) and reflectance (R) of PTFE in air as a function of PTFE thickness. These measurements establish the reliability of the employed experimental setup and will contribute to providing reference values for ALPINE LXe detector, which is currently under development for DM research. Particularly, ALPINE segmented TPC (Fig. 1a) features an unexplored PTFE–metal–PTFE interface (Fig. 1b), whose optical properties will enable a deeper understanding of light propagation in the detector volume and will support the optimization of the TPC segmented structure by minimizing photon leakages across the isolated optical regions.



(a) Vertical cross-section of the segmented TPC showing four optically isolated segments (PTFE) and single-piece electrode grids (metal).



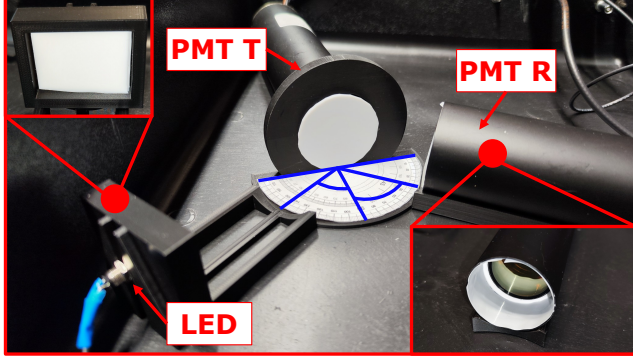
(b) PTFE-metal-PTFE interface to be considered for studying the optical properties of the segmented TPC layers.

Figure 1: Schematic representation of ALPINE detector design and its PTFE–metal–PTFE interface.

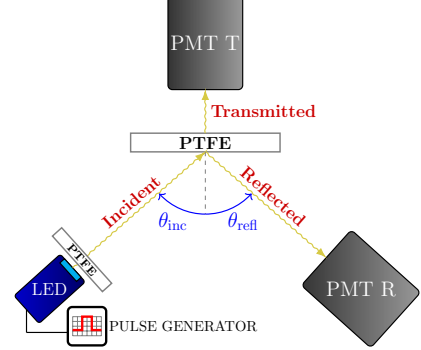
¹PTFE is also referred to as Teflon, its brand name.

2.2 Methodology

The experimental setup used to measure T and R of light at the PTFE–air interface, shown in Fig. 2, is located inside a dark box to prevent the intrusion of ambient light. The light source of the apparatus is produced by a blue² LED, which is driven by a pulse generator configured with a frequency of 600 Hz, a high level of 3.5 V, a low level of 2.0 V, 0.0 ns delay and a pulse width of 70 ns. Three PTFE rectangles of total thickness (4.65 ± 0.05) mm are placed in front of the LED to stabilize its signal in time and to filter out stray light.³ The emitted photons are detected by two HAMAMATSU PMTs, hereafter referred to as PMT T and PMT R, dedicated respectively to T and R measurements. Both PMTs are held firmly in place with 3D-printed holders (displayed in Fig. 2a) and are operated at 1300 V via a high voltage generator. Photon signals from PMTs are recorded using a CAEN digitizer, triggered by the TTL output of the pulse generator.



(a) Photograph of the apparatus.



(b) Schematic diagram of the apparatus.

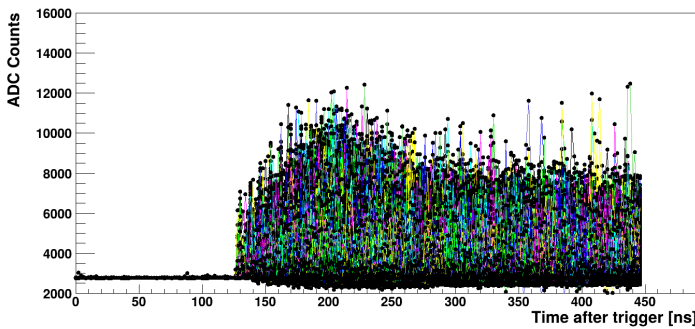
Figure 2: Employed experimental setup.

Several PTFE discs of three distinct thicknesses (0.20 mm, 1.55 mm, and 2.05 mm) are combined to obtain T and R measurements at eight different effective thicknesses, summarized in Tab. 1. As illustrated in Fig. 2a, these PTFEs are placed in front of PMT T, and are represented schematically by the horizontal PTFE rectangle in Fig. 2b.

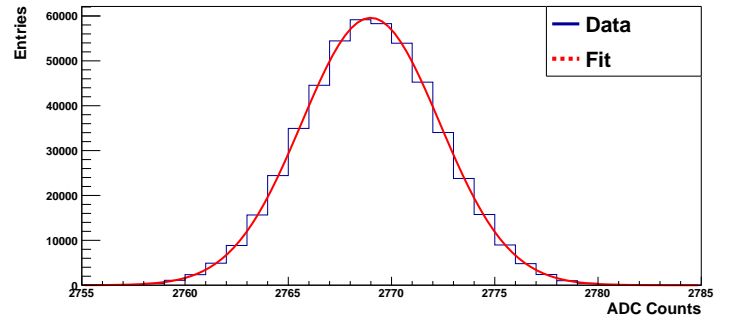
Effective thickness [mm]	0.20 mm discs	1.55 mm discs	2.05 mm discs
0.20 ± 0.05	1	0	0
0.80 ± 0.05	4	0	0
1.55 ± 0.05	0	1	0
2.05 ± 0.05	0	0	1
3.10 ± 0.05	0	2	0
3.60 ± 0.05	0	1	1
4.10 ± 0.05	0	0	2
5.15 ± 0.05	0	2	1

Table 1: Combination of PTFE discs used to achieve different effective thicknesses for T and R measurements.

In addition to investigating T and R dependence on PTFE thickness, the experimental setup in Fig. 2 allows to study their variation with respect to incidence (θ_{inc}) and reflection (θ_{refl}) angles, illustrated in Fig. 2b. In particular, measurements were performed at three angular configurations, fixing $\theta_{\text{inc}} = \theta_{\text{refl}}$ at 30° , 45° and 60° .



(a) A total of 60 000 raw digitized waveforms is acquired from each PMT, shown here superimposed.



(b) Electronic noise distribution data (blue) and relative Gaussian fit (red) extracted from the first 100 ns after the trigger.

Figure 3: Superimposed waveforms (expressed in ADC Counts) and corresponding noise characterization, both extrapolated from PMT signals. The trigger, provided by the TTL output of the pulse generator, corresponds to the activation of the blue LED.

The first step of the analysis is to extract valuable information from the light signals generated by the PMTs. For this purpose, a custom library based on C++ and ROOT is designed [17]. The digitized signal retrieved from each PMT is illustrated in Fig. 3a. No

²Blue light is used as proxy for LXe scintillation light [16].

³Note that this rectangular PTFE is not used to analyze T and R measurements. Its sole purpose is to attenuate the LED light.

physical insights can be extrapolated from this plot, except for the waveform baseline and the electronic noise distribution (shown in Fig. 3b), both evaluated in the first 100 ns after the trigger, that is before the onset of the dense forest of waveforms. Furthermore, as indicated in Fig. 3b, a Gaussian fit is performed over the electronic noise distribution in order to extract the noise width (σ_n) for each set of analyzed waveforms.

Once the value of σ_n is known, it serves as basis for the pulse-finding algorithm. For each waveform, the algorithm search for signal excursions above a threshold T' , set as $T' = 80 \cdot \sigma_n$. The choice of such a high threshold is justified by the relatively small baseline fluctuations represented by σ_n . To properly account for physical pulses, the waveform signal must not only exceed the threshold value, but also satisfy additional conditions once a candidate pulse maximum is detected. Firstly, the algorithm scans the ADC values around the identified peak to determine the pulse endpoints. Secondly, a minimum separation between consecutive pulses within the same waveform is required to avoid reconstruction artifacts arising from overlapping pulses. After the application of these criteria, valid pulses are identified, as shown in Fig. 4a. Additionally, to validate the correctness of the C++/ROOT software developed for data analysis, key pulse parameters are extracted, including the ones listed in Fig. 4b. For the development of this work, the most significant one is the pulse area A , being proportional to the number of photoelectrons N_{PE} generated by the PMTs. In turn, N_{PE} is proportional to the number of photons detected by the PMTs, N_γ , which is the parameter of interest for T and R .

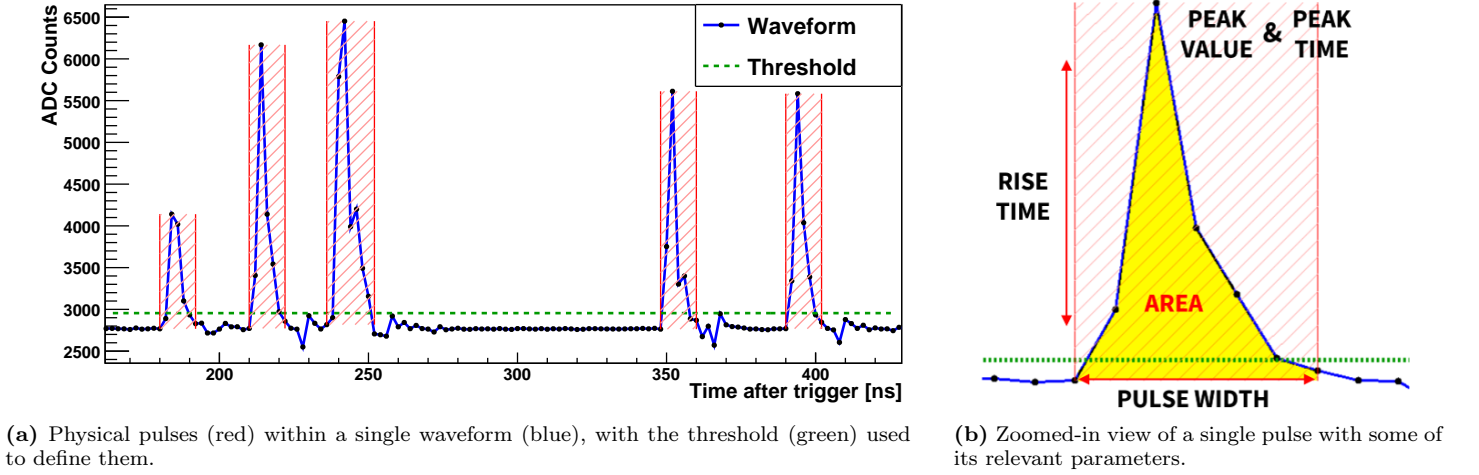


Figure 4: Illustration of physical pulses and their parameters.

To compute the pulse area A , PMT signals are integrated using the following discrete sum over the pulse width:

$$A = \sum_{\text{pulse width}} \left[\left(V_i^{\text{ADC}} - V_{\text{baseline}}^{\text{ADC}} \right) \cdot \Delta t \right], \quad (1)$$

where V_i^{ADC} and $V_{\text{baseline}}^{\text{ADC}}$ are respectively the ADC values of the i -th sample and of the baseline and Δt is the sampling period (2.0 ns for the employed digitizer). Using Eq. 1, one can plot the temporal distribution of pulse areas, shown in Fig. 5a. To calibrate the signal scale and to check that the experimental setup reliably detects single and possibly multiple photon events, the area in Fig. 5a expressed in [ADC·ns] is converted into the number of photoelectrons (PE), as illustrated in Fig. 5b. In the latter, two distinct peak centered around 1 and 2 PE are clearly visible, which correspond to the single- and double-PE events, respectively. Each PE peak in Fig. 5b is well described by a two-sided Gaussian fit, illustrated in the same plot.

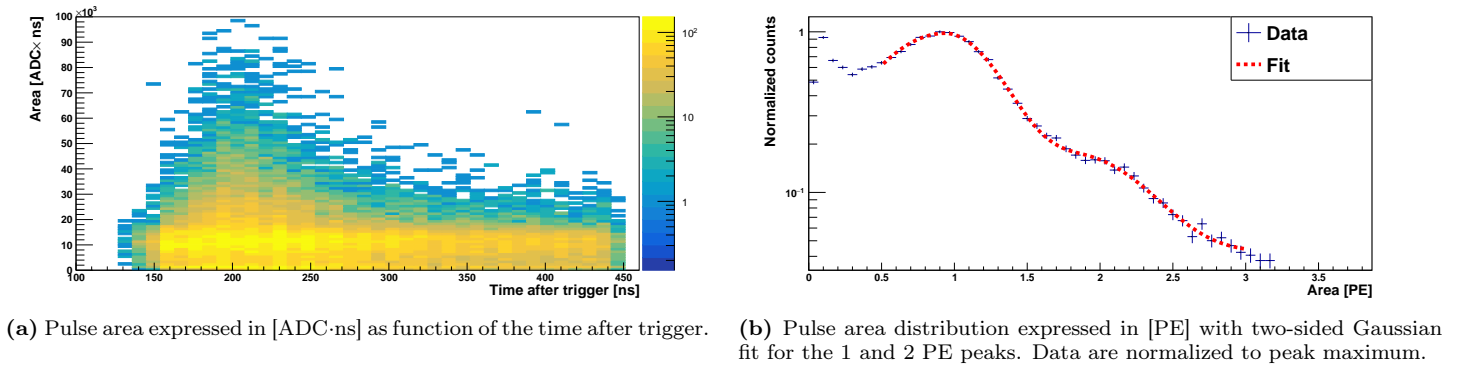


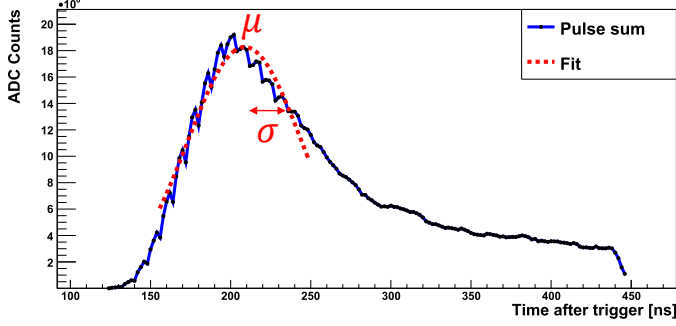
Figure 5: Pulse area distributions plotted using different unit of measurements.

The next step of the analysis is to divide waveforms into temporal regions relative to the trigger: a pre-integration region (containing possible baseline pulses), an integration region (where physical pulse areas will be summed to compute the collected light for T and R), and two post-integration regions (containing delayed pulses). To define the integration region, all pulses from Fig. 3a are summed to obtain the distribution in Fig. 6a, which is then fitted with a Gaussian function to extrapolate mean (μ) and width (σ). A first approach determines the integration window as the interval $[\mu - \sigma, \mu + \sigma]$; however, this method introduces a bias. This is evident by

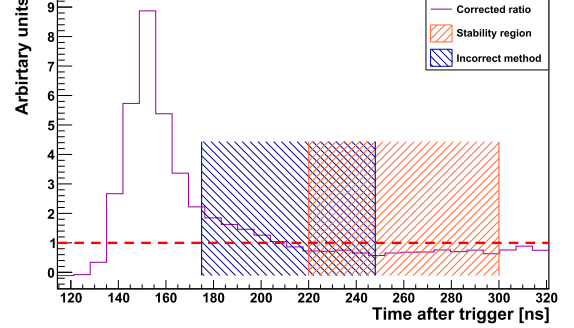
defining the histogram $H(t)$:

$$H(t) = \frac{S_R(t)}{S_I(t)}, \quad (2)$$

where $S_R(t)$ and $S_I(t)$ are respectively the pulse sum distributions of reflected⁴ and incident⁵ photons. Ideally, since $H(t)$ would represent an instantaneous ratio of R ,⁶ it should be constant in time, as no component in our experimental setup would cause R to change in time. However, by plotting $H(t)$ in Fig. 6b, time-dependent variations can be seen, probably introduced by different time responses of PMT T and PMT R. Thus, as illustrated in Fig. 6b, the integration window of the first approach (in blue) is not optimal, as it lies within an unstable range of $H(t)$. Conversely, a more reliable integration interval is chosen where $H(t)$ is stable (in orange), specifically within [220, 300] ns.



(a) Pulse sum graph obtained by summing all the pulses extracted from the superimposed waveform plot in Fig. 3a.



(b) $H(t)$ (purple) defined as indicated in Eq. 2. The blue region represents the integral window defined with the first, incorrect approach, while the orange region, falling within [220, 300] ns, corresponds to the chosen, unbiased integration region.

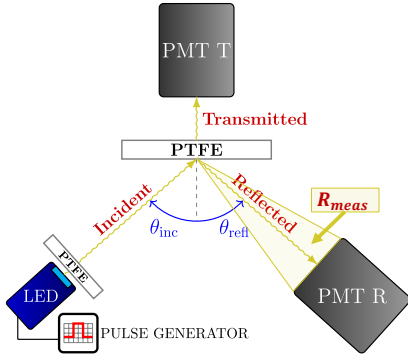
Figure 6: Plots used to define the integration region, which contains the physical pulses.

T and R are defined through the average PE rate r , computed summing pulse areas over the orange integration region shown in Fig. 6b:

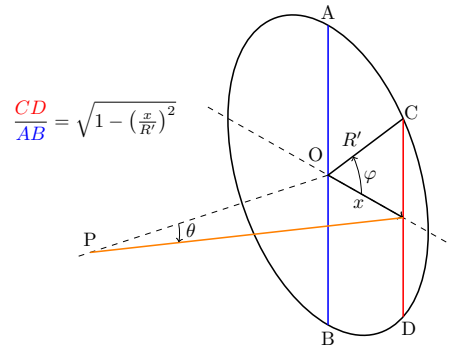
$$r = \frac{\sum_{\text{int}} (\text{Pulse area})}{\Delta t_{\text{int}} \cdot N_{\text{waveform}}}, \quad (3)$$

where $\Delta t_{\text{int}} = 80$ ns and $N_{\text{waveform}} = 60\,000$ are the time duration of the integration region and the number of analyzed waveforms, respectively. Using Eq. 3, T and R are finally obtained as follows:

$$T = \frac{r^{\text{transmitted}}}{r^{\text{incident}}} \quad \text{and} \quad R = \frac{r^{\text{reflected}} - r^{\text{direct}}}{r^{\text{incident}}}. \quad (4)$$



(a) Experimental setup with highlighted solid angle subtended by PMT R, within which R_{meas} is defined.



(b) Scheme illustrating the non-uniformity of light acceptance and the chord-diameter ratio CD/AB .

Figure 7: Scheme of the geometric acceptance corrections applied to R .

In contrast to T , R needs to be corrected to account for the geometric acceptance of PMT R. Specifically, measured reflectance R_{meas} is underestimated due to the limited solid angle subtended by PMT R's acceptance window, illustrated in Fig. 7a. To account for the absolute reflectance R_{true} , a geometrical correction factor f_{acc} is introduced, such that $R_{\text{meas}} \approx f_{\text{acc}} \cdot R_{\text{true}}$. f_{acc} is specified in Eq. 5 employing the reflectivity function F defined in [18], which models the specular and diffusive components of PTFE reflection:

$$f_{\text{acc}} = \frac{\int_{\theta_{\min}}^{\theta_{\max}} F(\theta_{\text{refl}}) d\theta_{\text{refl}}}{\int_{-90^\circ}^{90^\circ} F(\theta_{\text{refl}}) d\theta_{\text{refl}}} \quad \text{with} \quad F(\theta_{\text{inc}}, \theta_{\text{refl}}) = R_1(\theta_{\text{inc}}) e^{-\frac{\alpha^2(\theta_{\text{inc}}, \theta_{\text{refl}})}{2\sigma^2}} + R_2(\theta_{\text{inc}}) \cos(\theta_{\text{refl}}), \quad (5)$$

⁴Reflected photons are measured with PMT R after subtracting the photons traveling directly from the LED to PMT R. Direct photon contribution is particularly relevant at large θ_{inc} and θ_{refl} , as can be viewed from Fig. 2.

⁵Incident photons are measured with PMT T by removing the PTFE layer in front of it (see Fig. 2).

⁶Note that $H(t)$ is merely introduced as sanity check to define an unbiased integration region. It does not represent the physical reflectance.

where $[\theta_{\min}, \theta_{\max}]$ represents PMT R's acceptance window. Furthermore, since PMT R's aperture is circular (as shown in Fig. 2a), acceptance is not uniform across θ_{refl} , as can be seen in Fig. 7b. Consequently, photons at larger angles hit the circular aperture with lower probabilities. To include the circular hole correction, f_{acc} 's numerator is weighted with the chord-diameter ratio defined in Fig. 7b. Both geometrical corrections are finally accounted by f'_{acc} :

$$f'_{\text{acc}} = \frac{\int_{\theta_{\min}}^{\theta_{\max}} F(\theta_{\text{refl}}) \sqrt{1 - \left(\frac{\theta_{\text{refl}} - \theta_{\text{inc}}}{R'} \right)^2} d\theta_{\text{refl}}}{\int_{-90^\circ}^{90^\circ} F(\theta_{\text{refl}}) d\theta_{\text{refl}}}, \quad (6)$$

where $R' = 25^\circ \pm 1^\circ$ denotes the angular radius of PMT R. In the following, absolute R values (defined as $R = R_{\text{true}} \approx R_{\text{meas}}/f'_{\text{acc}}$) will be presented.

2.3 Results

Measurements of T and R at the different PTFE thicknesses listed in Tab. 1 are summarized in Tab. 2, with data divided by incidence and reflection angles $\theta_{\text{inc}} = \theta_{\text{refl}} = 30^\circ, 45^\circ$ and 60° . The corresponding dependencies of T and R on both thickness and angular configuration are illustrated in Fig. 8. As expected from [19], T decreases with thickness for all angles, and its values show compatibility with previous measurements [20]. Moreover, by fitting T data with a Beer-Lambert law $T = Ae^{-x/\lambda_T} + B$ (with x representing PTFE thickness), one can extrapolate the attenuation coefficient λ_T . As reported in the captions of Fig. 8a, Fig. 8b and Fig. 8c, corresponding respectively to the $30^\circ, 45^\circ$ and 60° configurations, the extracted λ_T values are mutually compatible across the three angular arrangements.

Contrary to T , R data shows a slightly increasing trend with thickness for all three configurations, in agreement with [16]. Although higher reflectivity values are observed at 60° for larger PTFE thicknesses, R does not reach the expected values reported in Sec. 2.1. This underestimation may be attributed to the lack of surface finish on the employed PTFE discs. Furthermore, R measurements are not fully consistent across $30^\circ, 45^\circ$ and 60° , confirming that reflectivity strongly depends on observation angles [21].

In addition to T and R , Fig. 8a, Fig. 8b and Fig. 8c also show the sum $T + R$, along with a constant fit to test experimental efficiency.⁷ As reported in the figure captions, the 30° and 45° constant fits are not compatible with the 60° configuration, indicating that the different angles do not share the same efficiency. Nevertheless, $T + R$ measurements exhibit a gradual decrease with thickness across all configurations, suggesting possible light absorption.

Thickness [mm]	30°		45°		60°	
	T	R	T	R	T	R
0.20 ± 0.05	0.467 ± 0.026	0.165 ± 0.023	0.604 ± 0.034	0.145 ± 0.032	1.429 ± 0.081	0.311 ± 0.283
0.80 ± 0.05	0.217 ± 0.012	0.308 ± 0.041	0.280 ± 0.016	0.280 ± 0.041	0.642 ± 0.036	0.386 ± 0.286
1.55 ± 0.05	0.196 ± 0.011	0.354 ± 0.046	0.248 ± 0.014	0.345 ± 0.045	0.541 ± 0.031	0.500 ± 0.290
2.05 ± 0.05	0.130 ± 0.007	0.382 ± 0.050	0.165 ± 0.009	0.369 ± 0.047	0.364 ± 0.021	0.683 ± 0.297
3.10 ± 0.05	0.105 ± 0.006	0.408 ± 0.053	0.126 ± 0.007	0.327 ± 0.044	0.301 ± 0.017	0.738 ± 0.299
3.60 ± 0.05	0.077 ± 0.004	0.389 ± 0.051	0.098 ± 0.006	0.352 ± 0.046	0.239 ± 0.014	0.675 ± 0.297
4.10 ± 0.05	0.065 ± 0.004	0.431 ± 0.056	0.080 ± 0.005	0.426 ± 0.051	0.185 ± 0.010	0.914 ± 0.306
5.15 ± 0.05	0.058 ± 0.003	0.422 ± 0.055	0.069 ± 0.004	0.349 ± 0.045	0.155 ± 0.009	0.706 ± 0.298

Table 2: T and R values at different PTFE thicknesses and angular configurations.

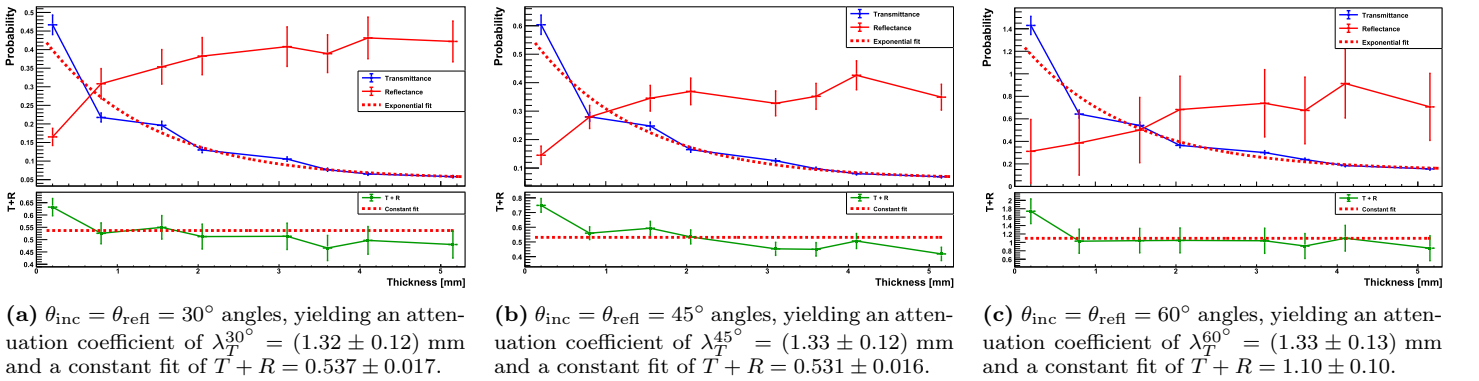


Figure 8: T , R and $T + R$ plots at different PTFE thicknesses and angular configurations with Beer-Lambert and constant fits. T and R uncertainties stem from errors on the fitted mean of the 1 PE peak in Fig. 5b (associated with the [ADC·ns] to [PE] conversion) and of the waveform area distribution (not reported). R is also influenced by parameter errors in Eq. 6, some drawn from [18].

To conclude, further studies are required to account for systematic uncertainties that strongly affect reflectance, such as PTFE density, temperature, surface finish, manufacturing process and purity [22]. Finally, the reproduced T and R at PTFE–air interface will be employed to test the PTFE–metal–PTFE for optimizing ALPINE detector and the light tightness of its segmented TPC.

2.4 Your contributions as a S3P3 student

My personal contributions to the project include the development of the C++/ROOT analysis software employed for the pulse-finding algorithm and for pulse integration (Fig. 3, Fig. 4 and Fig. 6), the calibration of PMT T and PMT R single- and double- PE peaks (Fig. 5), the data acquisition for all PTFE sample thicknesses and angular configurations and the final analysis of T and R (Fig. 8), including the application of the geometric acceptance corrections (Fig. 7).

⁷That is, whether T and R add up to unity.

References

- [1] V. C. Rubin, W. K. Ford Jr., and N. Thonnard. “Extended rotation curves of high-luminosity spiral galaxies. IV. Systematic dynamical properties, Sa through Sc”. *Astrophys. J. Lett.* 225 (1978), pp. L107–L111.
- [2] P. A. R. Ade et al. “Planck2013 results. I. Overview of products and scientific results”. *Astronomy and Astrophysics* 571 (Oct. 2014), A1.
- [3] T. M. Undagoitia and L. Rauch. “Dark matter direct-detection experiments”. *Journal of Physics G: Nuclear and Particle Physics* 43.1 (Dec. 2015), p. 013001.
- [4] K. GRIEST. “The Search for the Dark Matter: WIMPs and MACHOs”. *Annals of the New York Academy of Sciences* 688.1 (June 1993), 390–407.
- [5] J. Angle et al. “First Results from the XENON10 Dark Matter Experiment at the Gran Sasso National Laboratory”. *Physical Review Letters* 100.2 (Jan. 2008).
- [6] V. N. Lebedenko et al. “Results from the first science run of the ZEPLIN-III dark matter search experiment”. *Physical Review D* 80.5 (Sept. 2009).
- [7] D. Akerib et al. “Results from a Search for Dark Matter in the Complete LUX Exposure”. *Physical Review Letters* 118.2 (Jan. 2017).
- [8] J. Jortner et al. “Localized Excitations in Condensed Ne, Ar, Kr, and Xe”. *The Journal of Chemical Physics* 42.12 (June 1965), pp. 4250–4253.
- [9] N. Basov et al. “Luminescence of condensed Xe, Kr, Ar and their mixtures in vacuum region of spectrum under excitation by fast electrons”. *Journal of Luminescence* 1-2 (1970), pp. 834–841.
- [10] T. L. Collaboration et al. “LUX-ZEPLIN (LZ) Conceptual Design Report”. 2015.
- [11] V. Weidner and J. Hsia. “Reflection properties of pressed polytetrafluoroethylene powder”. *Journal of the Optical Society of America* 71 (July 1981), pp. 856–861.
- [12] D. Akerib et al. “The Large Underground Xenon (LUX) experiment”. *Nuclear Instruments and Methods in Physics Research Section A: Accelerators, Spectrometers, Detectors and Associated Equipment* 704 (Mar. 2013), pp. 111–126.
- [13] F. Neves et al. “Measurement of the absolute reflectance of polytetrafluoroethylene (PTFE) immersed in liquid xenon”. *Journal of Instrumentation* 12.01 (Jan. 2017), P01017–P01017.
- [14] E. Aprile et al. “Material radioassay and selection for the XENON1T dark matter experiment”. *The European Physical Journal C* 77.12 (Dec. 2017).
- [15] J. Haefner et al. “Reflectance dependence of polytetrafluoroethylene on thickness for xenon scintillation light”. *Nuclear Instruments and Methods in Physics Research Section A: Accelerators, Spectrometers, Detectors and Associated Equipment* 856 (June 2017), pp. 86–91.
- [16] S. Ghosh et al. “Dependence of polytetrafluoroethylene reflectance on thickness at visible and ultraviolet wavelengths in air”. *Journal of Instrumentation* 15.11 (Nov. 2020), P11031–P11031.
- [17] S. Pasquini. “UZH Summer Student Program”. Version v1.1.0. Sept. 2025.
- [18] C. Levy. “Light Propagation and Reflection off Teflon in Liquid Xenon Detectors for the XENON100 and XENON1T Dark Matter Experiment”. PhD thesis. U. Munster, 2014.
- [19] D. Cichon et al. “Transmission of xenon scintillation light through PTFE”. *Journal of Instrumentation* 15.09 (Sept. 2020), P09010–P09010.
- [20] B. Tsai et al. “A Comparison of Optical Properties between High Density and Low Density Sintered PTFE”. *Proceedings of SPIE - The International Society for Optical Engineering* 7065 (Aug. 2008).
- [21] Y. Barnes, A. Parr, and E. Early. “Spectral Reflectance”. en. 1998.
- [22] C. F. P. d. Silva. “Study of the Reflectance Distributions of Fluoropolymers and Other Rough Surfaces with Interest to Scintillation Detectors”. PhD Thesis. Universidade de Coimbra, 2009.